Heteroatomic interface engineering of MOF-derived metal-embedded P and N-codoped Zn node porous polyhedral carbon with enhanced sodium-ion storage

Siqi Zhu[a,#], Hong Yin[a,#], Yatong Wang[b,#], Kwan San Hui[c,*], Xi-Lin Wu[d], Wenjie Mai[e], Xiaoting Hong[f], Fuming Chen[g,*], Kwun Nam Hui[a,*]

[a] Joint Key Laboratory of the Ministry of Education, Institute of Applied Physics and Materials Engineering, University of Macau, Avenida da Universidade, Taipa, Macau SAR 999078, China.

[b] College of Physics and optoelectronics, Taiyuan University of technology, Taiyuan, 030024, China.

[c] Engineering, Faculty of Science, University of East Anglia, Norwich, NR4 7TJ, United Kingdom

[d] College of Geography and Environmental Science, Zhejiang Normal University, Jinhua, 321004, China.

[e] Siyuan Laboratory, Guangdong Provincial Engineering Technology Research Center of Vacuum Coating Technologies and New Energy Materials, Department of Physics, Jinan University, Guangzhou 510632, China.

[g] School of Physics and Telecommunication Engineering, South China Normal University, Guangzhou 510006, China.

[#] These authors contributed equally

[*] Corresponding author

Kwan San Hui, E-mail: k.hui@uea.ac.uk

Fuming Chen, E-mail: fmchen@m.scnu.edu.cn

Kwun Nam Hui, E-mail: bizhui@um.edu.mo

ABSTRACT

Amorphous-ordered mesoporous carbon materials are regarded as the most promising anode candidate for sodium-ion batteries (SIBs) owing to their eco-friendliness, abundance, thermal stability, and low price. However, poor rate, low initial Coulombic efficiency, and poor cycling performance have been the major challenges of SIBs. Herein, we successfully constructed robust phosphorus and nitrogen-codoped Zn node porous polyhedral carbon polyhedron (P-N-Zn-C). The as-prepared P-N-Zn-C anode delivers outstanding electrochemical performance and ultrahigh stability and has achieved a remarkable capacity of 460 mA h g^{-1} at 100 mA g^{-1}, long-term cycling stability of up to 100 cycles, and an excellent rate performance even at a current density of up to 1000 mA g^{-1}. The remarkable performance can be ascribed to the enlarged interlayer distances of carbon and the existence of Zn node, which facilitate the insertion–extraction of Na ions. The first-principle density functional theory calculations revealed that the presence of P, N, and Zn could reduce the band gaps between the valence and conduction bands and accelerate the electron transfer reaction rate. This study underscores the potential importance of heteroatom doping as an effective strategy for improving the performance of carbon electrode materials.

Keywords: mesoporous, heteroatom, Zn node, phosphorus, sodium-ion batteries.

1. INTRODUCTION

Lithium-ion batteries (LIBs) have achieved huge commercial success in the energy storage device market. However, the supply deficit and high cost of lithium resource hinder LIBs' further development.[1-2] Sodium and lithium have the most similar properties because they belong to the same group in the periodic table. However, sodium has almost unlimited resources and a cheaper price compared with lithium. Hence, sodium-ion batteries (SIBs) have been reported as the best hopeful candidate for next-generation full-scale energy conversion and storage system.[2-3] Na ion has a larger radius (1.02 Å) than Li ion (0.76 Å); thus, Na ion is harder to intercalate into electrode materials for SIBs. Besides, the lower standard electrode potential of Na^+/Na (-2.71 V) results in relative low energy density compared with LIBs and hinders its commercial application. Thus, finding an appropriate electrode material to provide enough space for relieving the volume expansion for Na-ion storage and transport will be the biggest challenge.[4] Metal oxides, alloys, and carbonaceous materials have been explored as anode materials for SIBs.[5-9] Similar to anode materials for LIBs, carbonaceous materials are also the most attractive candidate for SIBs because of their eco-friendliness, abundance, thermal stability, and low price. Therefore, tremendous carbon nanomaterials have been proposed, including hard carbon, carbon sheets, carbon fibers, carbon nanotubes, and graphene.[10-18]

However, carbon-based materials have two main disadvantages: low initial Coulombic efficiency (CE) and poor cycling performance. Moreover, Na ions can hardly intercalate into common graphite-based anode materials because of their narrow

interlayer distance and larger ionic radius, which hinder their further application. Doping heteroatoms (such as N, P, S, and B) in host materials is an effective approach to enlarge the specific surface area and interlayer spacing of host materials. Doping can also improve the electrical conductivity and enhance the absorbability of Na ion in the sodiation/desodiation process.[20-23] Among heteroatom-doped materials, N-doped carbonaceous materials, such as N-doped carbon fibers,[17, 24-26] N-doped carbon nanosheets,[27] and N-doped graphene,[28] have been extensively investigated and remarkably improved the reactivity and electronic conductivity of anode materials for SIBs.[29]

As a subclass of metal-organic frameworks, zeolitic imidazolate frameworks (ZIFs) are based on simple zeolite structures, which consist of metal nodes and methylimidazole ligand. Porous ZIFs could transfer into N-doped porous carbon by direct carbonization because of their high nitrogen contents. N-doped porous carbon matrix is generated by the pyrolysis and aggregation of organic ligands during the unique *in situ* carbonization process under gas-protected atmosphere. Most importantly, the N-doped porous carbon matrix derived from organic frameworks fully encapsulates Zn metal node and active sites to dramatically facilitate ion/electron transmission and prevent the electrode materials from destruction during the sodiation/desodiation process.[30] The pyrolysis of ZIF-8 polyhedrons also serves as an effective way to obtain N-doped Zn node porous carbon (N-Zn-C) materials.[31-32] However, few studies have reported the attainment of heteroatom-doped Zn-node carbon matrix through the pyrolysis of ZIFs. N-Zn-C materials retain the structural features of parent ZIF-8

particles. ZIF-8 particles are consisted of a mass of graphene-analogous particles,[33] which can provide rich active sites for implanting heteroatoms. Phosphorus has the same number of valence electrons as nitride[34-35] and a much greater radius than carbon; hence, P-doping in carbon drives local structural distortion in carbon hexagonal framework and enlarges the basal plane spacing, which could facilitate Na-ion transport.[28, 36-38]

Here, we reported the construction of a well-defined phosphorus and nitrogen-codoped Zn node porous polyhedral carbon material (P-N-Zn-C) through *in situ* carbonization process derived from ZIFs to wrap and interconnect monodispersed Zn nanoparticles under Ar/H$_2$ atmosphere. As an anode material for SIBs, the P-N-Zn-C composite exhibited an excellent capacity of 460.4 mA h g^{-1} at 100 mA g^{-1} after 100 cycles and delivered 130 mA h g^{-1} after 2500 cycles at 1A g^{-1}. Thus, the P-N-Zn-C composite has superior cycling stability and rate capability for SIBs. The improved capacity and cycling stability are attributed to the unique porous polyhedral structure of the composite. The porous composite increased the electrode-electrolyte contact area, accelerated the ion/electron transform, and improved the pseudocapacitive behavior of the electrode during the Na-ion intercalation process.[39-40] Experimental and density functional theory (DFT) data revealed that the existence of P, N, and Zn node can substantially enhance sodium storage performance.

2. EXPERIMENTAL SECTION

ZIF-8 Synthesis

Zn(CH₃COO)₂·2H₂O (498.1 mg, 99%; Aladdin) was added in 60 mL of methanol (99.5%, Sinopharm group, MeOH) and subsequently was poured into 60 mL of MeOH with 1968 mg 2-methylimidazole (98%, Aladdin). The mixture was continuously stirred at 25 °C for 24 h and allowed to stand for 6 h. The deposits were washed with MeOH several times to obtain white polyhedral ZIF-8.

N-Zn-C and N-C Syntheses

ZIF-8 precursor was transferred into a ceramic boat and heated to 350 °C in Ar/H₂ (90%/10%) for 1.5 h with a heating rate of 2 °C min⁻¹. Then, the temperature was further elevated to 650 °C at Ar/H₂ (90%/10%) for 2 h. Finally, the porous polyhedral N-Zn-C material can be obtained after the heat treatment processes.

The N-Zn-C composite was etched with concentrated hydrochloric acid (37%, Sinopharm group) for 12 h to remove Zn node and then washed with ethanol and deionized water several times to obtain N-doped porous carbon (N-C).

P-Zn-N-C Synthesis

Commercial red phosphorous (150 mg, purity ≥ 99%, Sinopharm) and the as-prepared N-Zn-C (30 mg) were mixed and placed in a ceramic boat, then heated to 650 °C at 2 °C min⁻¹, and further heated at 650 °C for 2 h. Afterward, the temperature was decreased to 260 °C and held at this temperature for 24 h to remove the residual red phosphorous. The ceramic boat was naturally cooled to room temperature, and the mixture was washed with CS₂ (purity ≥ 98%, Sinopharm) to remove the white

phosphorous and other phosphates generated during the condensation process and dried under vacuum to obtain polyhedral P-N-Zn-C.

Material Characterization

Horiba LABHRev-UV Raman spectrometer with an argon ion laser (λ=630 nm) was used to collect the Raman spectra. Powder X-ray diffraction (XRD) (Rigaku Smart lab 9000W) with Cu Kα1 radiation (λ=1.54056 Å) was used to characterize the crystal structures. Microscopic morphologies were conducted by field-emission scanning electron microscopy (FESEM, Zeiss Zigma) and transmission electron microscopy (TEM, FEI Talos F200X). N_2 adsorption/desorption curves were collected on a Micromeritics 3Flex physisorption surface area analyzer at liquid nitrogen temperature. The valence bond and component of the composites were tested by X-ray photoelectron spectrometry (XPS) using a Thermo ESCALAB 250 instrument with Al Kα (1486.6 eV) as the X-ray source. Thermal gravimetric analysis (TGA) was conducted on a TA Instruments SDT-Q600 thermal analyzer.
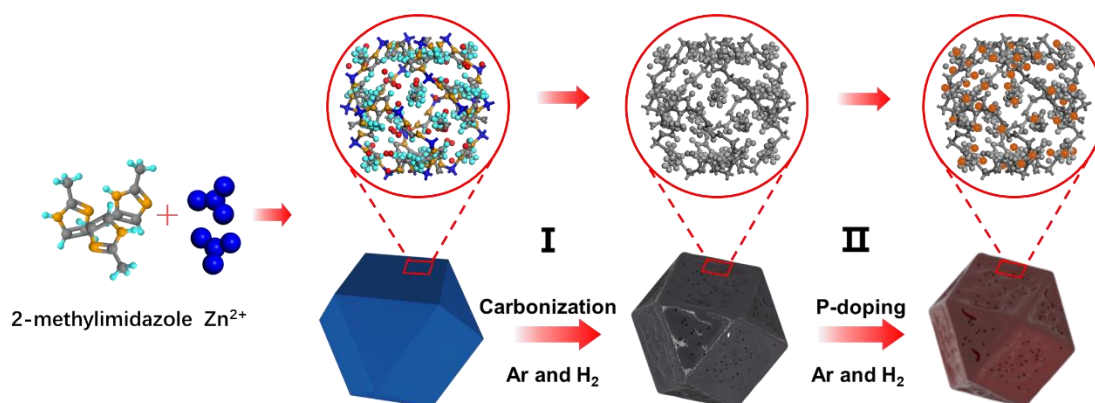
Electrochemical Measurements

The electrodes consisted of active materials, super P (Sigma), and carboxymethyl cellulose binder (purity $\geq$ 99%, Sinopharm) with a ratio of 8:1:1. The active mass loading of the electrode was around 1.13 mg cm^{-2}. Cu foil was used as the current collector, and Na foil was used as the counter electrode. All the cells were fabricated in a glove box with moisture and oxygen concentration below 0.1 ppm. Charge/discharge measurements were conducted using a LAND CT2001A cell test instrument. Cyclic voltammetry (CV) tests were performed on a CHI 760E electrochemical workstation.

Computational Methods

First-principle calculations based on DFT were performed in the Vienna Ab initio Simulation Package. The projected-augmented-wave method was chosen to describe the electron-ion interaction. The exchange-correlation interaction functional was the generalized gradient approximation in the Perdew-Burke-Ernzerhof functional. The energy cutoff of the plane waves was set to 500 eV and the vacuum separation between two nanosheets was set to 30 Å to avoid the virtual interactions caused by the use of periodic boundary conditions. The optimization of underlying structure was performed using the conjugate gradient method, and the convergence criterion was set to 10^{-6} eV/cell in energy and 0.01 eV/Å in force. The Brillouin zone was integrated using a $10 \times 12 \times 1$ Γ-centered k-mesh according to the Monk horst-Pack method during the structure relaxation and a denser $20 \times 24 \times 1$ MP mesh for the calculation of electronic property.[41] The van der Waals (vdW) correction DFT-D2 proposed by Grimme was chosen to describe the long vdW interaction for the adsorption of small molecules.

3. RESULT AND DISSCUSSION

Scheme 1. Schematic illustration of the preparation of the P-N-Zn-C composite.

Scheme 1 shows the schematic illustration of the preparation procedure of the P-N-Zn-C composite. The N-Zn-C composite with well-defined pore size (~320 nm) and distribution was prepared by directly annealing ZIF-8 (**Figure S1**) in Ar/H_2 mixed atmosphere. All the peaks of the XRD profiles (**Figure S2**) well matched the simulated pattern of ZIF-8. During heat treatment, the H_2 in the Ar/H_2 mixed atmosphere promoted the formation of hierarchical hollow-structured frameworks and facilitated the quick formation of metallic Zn node,[42] which plays a critical role in the formation of the N-Zn-C structure. N-Zn-C was annealed in red phosphorous in a gas–solid reaction process to obtain the P-N-Zn-C composite and were further condensed on the P-N-Zn-C composite under heating treatment in Ar/H_2 at 650 °C. Unconverted white phosphorous and other phosphate were removed with CS_2, ethanol, and deionized water, and P source was embedded in the N-Zn-C composite.
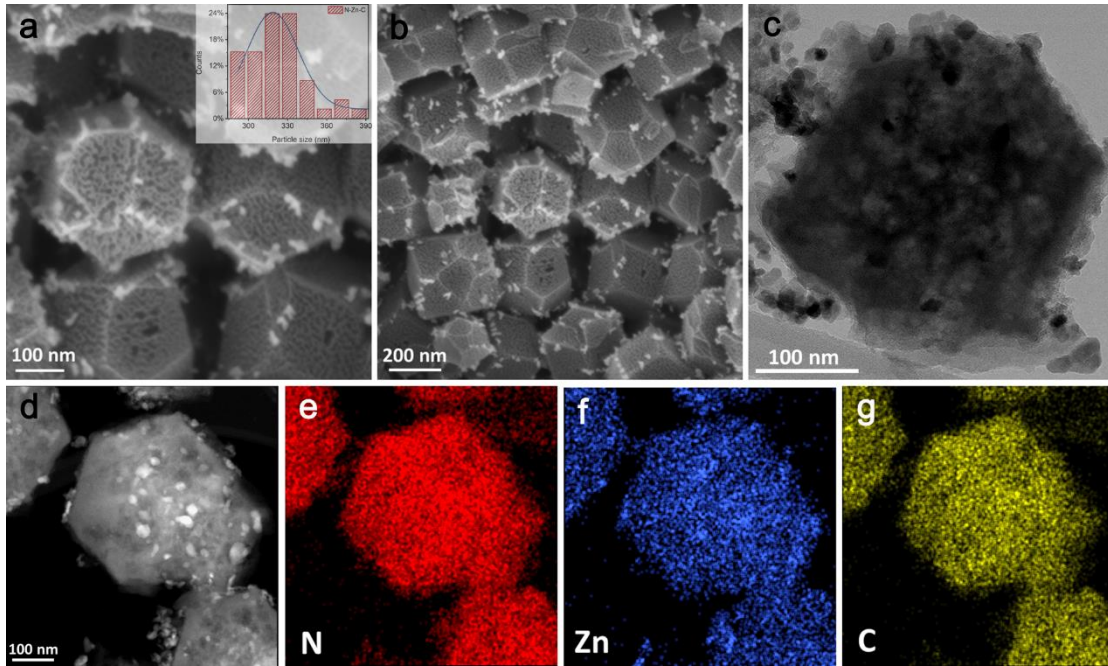
Figure 1. (a, b) SEM and (c) TEM images of the N-Zn-C composite; inset in (a) shows the particle size distribution. (d-f) HAADF-STEM images with the corresponding element distribution images of N-Zn-C composites.

The morphology and microstructure of the obtained N-Zn-C composite were investigated using FESEM and TEM. **Figures 1a-c** show that the N-Zn-C composite possessed many nanopores over the entire particle surface after calcination under Ar/H_2 atmosphere. The high-angle annular dark-field scanning transmission electron microscopy (HAADF-STEM) image and corresponding energy-dispersive X-ray spectroscopy (EDS) mapping images indicated the homogeneous distribution of N, Zn, and C in the whole composite (**Figures 1d-g**). Some of the outer Zn volatilized and escaped from the structure when the temperature rose to the melting point of Zn. The organic ligands around Zn collapsed and evaporated more quickly than Zn during pyrolysis and finally formed the Zn particles on the surface.[43]
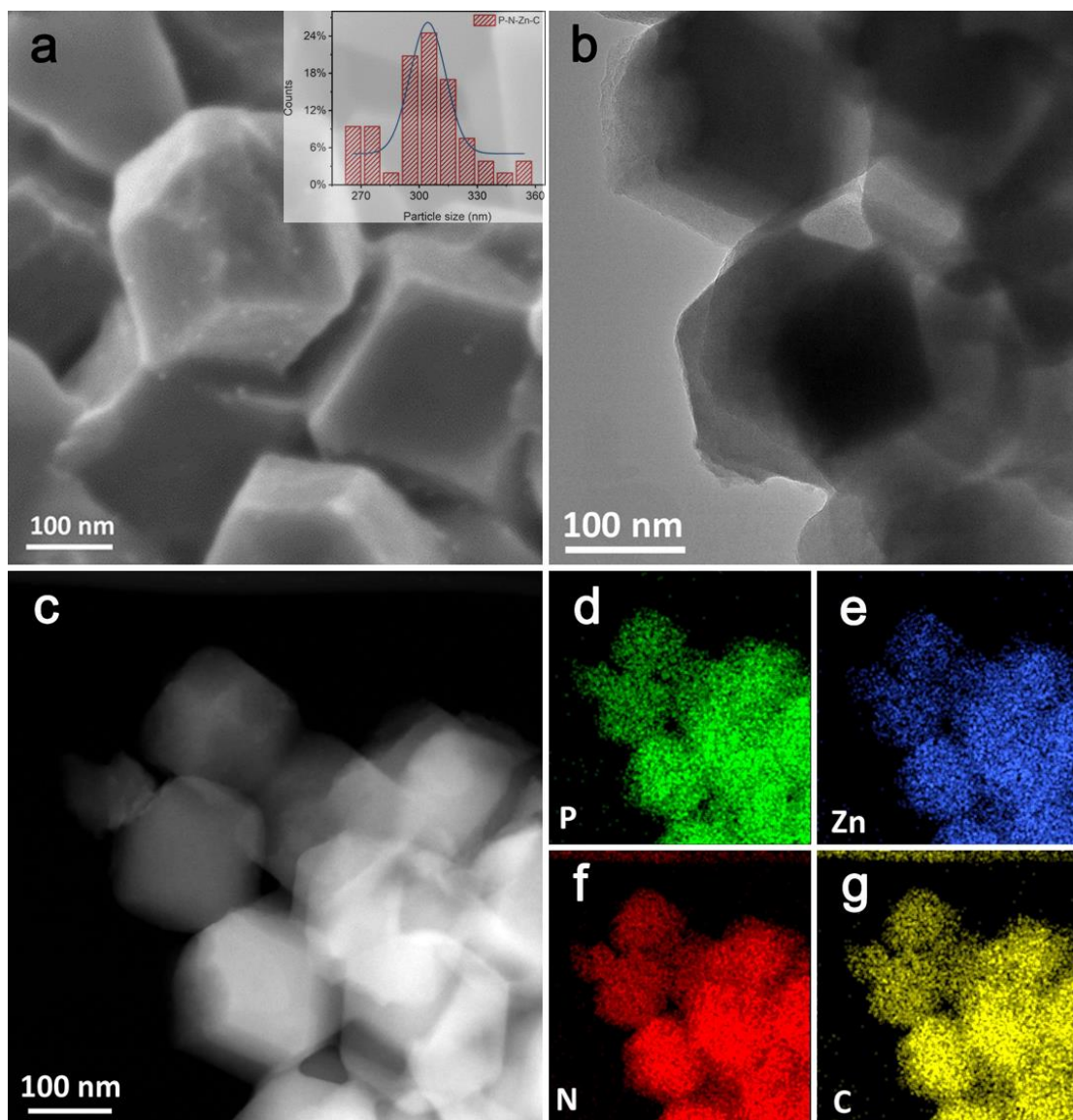
Figure 2. (a) SEM image of the P-N-Zn-C composite; inset in (a) shows the particle size distribution. (b) TEM and (c-g) HAADF-STEM images with the corresponding element distribution images of the P-N-Zn-C composites.

The size average of the as-synthesized P-N-Zn-C composite was about 310 nm, which is smaller than that of N-Zn-C particle (**Figures 2a-b**) because the outer layer was distorted and broken during heat treatment.[44] The HAADF-STEM image and corresponding EDS mapping images indicated the homogeneous distribution of P, N, Zn, and C in the whole composite (**Figures 2d-g**). The Brunauer-Emmett-Teller data

(**Figure S3**) were measured and revealed that the P-N-Zn-C composite has a larger surface area of 550.6 $m^2 g^{-1}$ compared with that of N-Zn-C (331.3 $m^2 g^{-1}$). The pore size distribution plot indicates that the pore sizes of N-Zn-C and P-N-Zn-C are 6.68 and 2.52 nm, respectively. The micropores in the P-N-Zn-C composite could efficiently decrease the diffusion length for ions/electrons and thus largely improve their electrochemical properties. Furthermore, the porous structure and carbon matrix of the P-N-Zn-C composite can accommodate the volume expansion and release the mechanical stress, which benefits the stability of the structure after long-time sodiation/desodiation processes.[45, 46]

XRD results revealed the crystal structure and phase purity of the P-N-Zn-C composite (**Figure 3a**). The broad peaks of P-N-Zn-C and N-Zn-C at 26° and the implicit peak at 44° correspond to the (002) and (010) planes, respectively, which indicate the presence of amorphous carbon feature. The (002) diffraction peak around 26° slightly shifted to lower 2θ values and became broader after P doping in N-Zn-C; these changes indicate that more defects were induced.[47] No diffraction peak from Zn metal was observed because of the encapsulation of Zn metal node into the thick carbon matrix. The high-resolution transmission electron microscopy (HR-TEM) image (**Figure S4**) of P-N-Zn-C revealed that the lattice spacing distance of amorphous carbon increased from 0.32 nm to 0.36 nm, which is in good agreement with the XRD. Based on TGA (**Figure S5**), the first weight loss before 200 °C is attributed to the loss of water and methanol. The weight loss before 419.5 °C is attributed to the carbonization of the methylimidazole ligand. The weight loss after 419.5 °C is due to the evaporation of Zn

and the carbonization of residual organic materials. The weight loss beyond 650 °C is due to the evaporation of Zn and the decomposition of the ZIF-8 structure.

The valence states of the P-N-Zn-C and N-Zn-C composites were analyzed by XPS. The full spectrum of the P-N-Zn-C composite (**Figure S6**) confirmed the existence of P, N, Zn, and C atoms. The obtained signal of the P 2p XPS spectrum in **Figure 3b** demonstrates the P-N bond at 133.7 eV and the P-C bond at 133.2 eV.[48] According to a previous report,[49] P heteroatom preferentially substitutes the corner of C site to form P-N bonds with a phosphorization treatment, and the band of 135.0 eV is assigned to the oxidation of phosphorus resulting from the superficial oxidation after exposure to air.[50] As shown in **Figure 3c**, the C 1s spectrum contains the peaks of sp^2 carbon C-C at 284.6 eV, sp^3 C-N/C-P bond at 285.7 eV, and C=O bond at 287.8 eV.[41, 51-52] The defect level is reflected by the sp^3 content. The value of sp^2/sp^3 for the P-N-Zn-C composite decreased from 1.35 to 0.92 compared with the N-Zn-C composite. This decrease indicates more defects in the P-N-Zn-C composite. As shown in **Figure 3d**, the high-resolution N1s spectra of the P-N-Zn-C and N-Zn-C composites can be fit well with four kinds of N species, namely, N-sp^3C (398.5 eV), N-Zn (399.7 eV), pyrrolic N (400.6 eV), and graphitic N (401.4 eV).[53-54] The high-resolution XPS spectra of Zn 2p (**Figure 3e**) in P-N-Zn-C shifts to a higher binding energy and displays a reduction in the fraction of low binding energy component compared with that in N-Zn-C composites. These changes imply that surface defects, such as vacancies in graphite and interstitial metal, dramatically increase after phosphorus doping.[55] The Fourier-transform infrared (FT-IR) spectra of P-N-Zn-C and N-Zn-C composites are

displayed in **Figure S7**. In contrast to N-Zn-C, the emergence of P-N bond at 930-1110 cm^{-1} and P-C bond at 650-795 cm^{-1} and the disappearance of the C≡C stretching bands (2190-2260 cm^{-1}) after phosphorization. According to FT-IR data, the P-N-Zn-C composite was successfully functionalized with the phosphorous functional groups. The crystallinity of the carbon substrate was further investigated by Raman spectroscopy. Overall, two first-order Raman bands exist, namely, the D band located at 1325 cm^{-1} and the G band at 1573 cm^{-1}. The ratio of the intensities of the D- and G-Raman peaks (I_D/I_G) could gauge the amount of structural defects. The Raman spectra (**Figure 3f**) revealed I_D/I_G values of 1.34 for the N-Zn-C composite and 1.41 for the P-N-Zn-C composite. The increase in I_D/I_G indicates an increase in defects.[56] This result is consistent with the XPS results. The Raman spectra (**Figure 3f**) and XPS spectrum of C1s (**Figure 3c**) suggest that more active sites and defects are caused by the co-coordination among Zn, P, and N-doped carbon. These sites and defects are beneficial to the enhanced electronic performance of carbon and the facilitation of the charge transfer process and the electrostatic adsorption of Na ions during the sodiation/desodiation process.
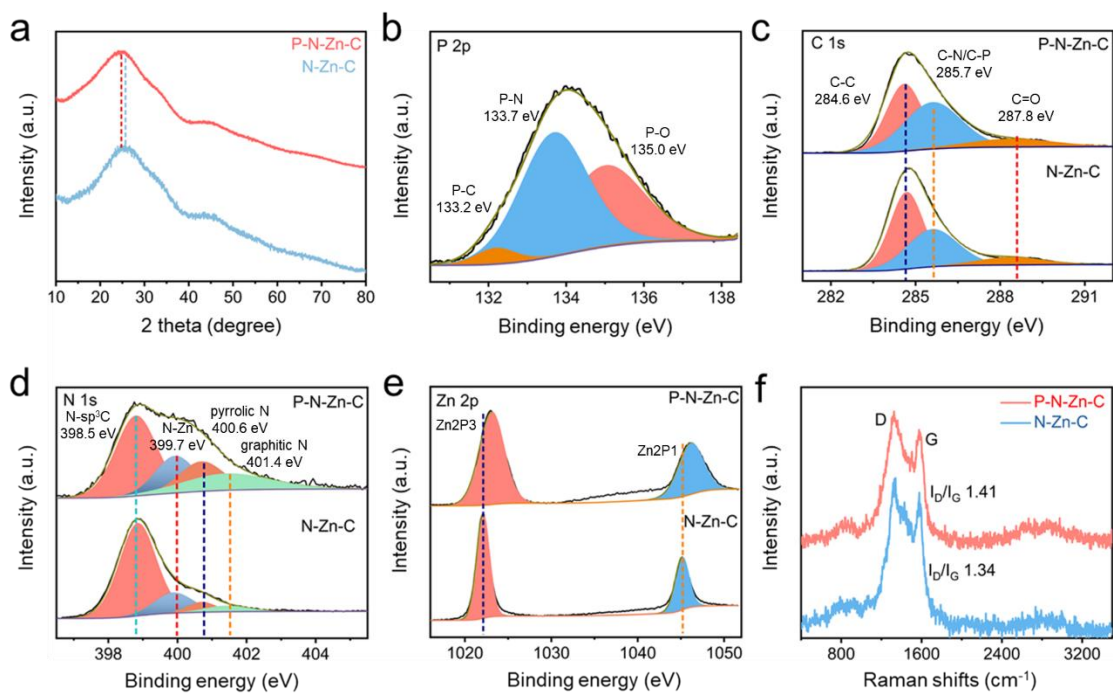
Figure 3. (a) XRD pattern of the P-N-Zn-C and N-Zn-C composites. XPS spectra of (b) P 2p in the P-N-Zn-C composite and (c) C 1s, (d) N 1s, and (e) Zn 2p in the P-N-Zn-C and N-Zn-C composites. (f) Raman spectra of the P-N-Zn-C and N-Zn-C composites.

The as-prepared P-N-Zn-C and N-Zn-C composites were employed as anode materials for SIBs to demonstrate sodium storage properties. **Figure 4a** shows the typical charge/discharge curves of the P-N-Zn-C electrode at 500 mA g^{-1}. The initial discharge capacity of 847.3 mA h g^{-1} and the charge capacity of 423.6 mA h g^{-1} yielded a CE of 50%. The initial CE of the P-N-Zn-C electrode was higher than that of the N-Zn-C electrode (27.3%). The overlapping of the charge/discharge curves in the following cycles suggesting the good stability and remarkable reversibility of Na-ion insertion/extraction in the P-N-Zn-C electrode. Notably, the sloping voltage profiles under galvanostatic mode exhibit a possible pseudocapacitive behavior.[57] **Figure 4b** shows the cycling performances of the P-N-Zn-C and N-Zn-C electrodes at 100 mA g^{-1}. The first discharge and charge capacities of the P-N-Zn-C electrode were 883.3 and

535.5 mA h g^{-1}, respectively, with a high initial CE of 60.6%. The irreversible capacity loss is caused by the electrolyte side reaction with Na and the partially irreversible Na-ion trapping in the amorphous carbon and solid electrolyte interphase (SEI).[55] By contrast, the N-Zn-C electrode delivered an initial discharge and charge capacities of 338.5 and 137.3 mA h g^{-1}, respectively, with a lower initial CE of 40.6%. The N-Zn-C electrode showed a rapid capacity loss in discharge capacity and only delivered 149.3 mA h g^{-1} at 100 mA g^{-1} after 100 cycles with a lower retained capacity of 44%. The P-N-Zn-C electrode maintained a stable discharge capacity of 460.4 mA h g^{-1} at 100 mA g^{-1} after 100 cycles with a retained capacity of 52%. The good cycling stability of the P-N-Zn-C electrode is attributed to its integral structural stability with phosphorus doping carbon-shell modification. In addition, the higher discharge capacity of the P-N-Zn-C electrode than the theoretical specific capacity of graphite (284 mA h g^{-1})[55] could be ascribed to the formation of an electroactive polymeric gel-like film on the surface of hollow porous structure, as well as the insertion of Na ions into interfacial storage.[58, 59]
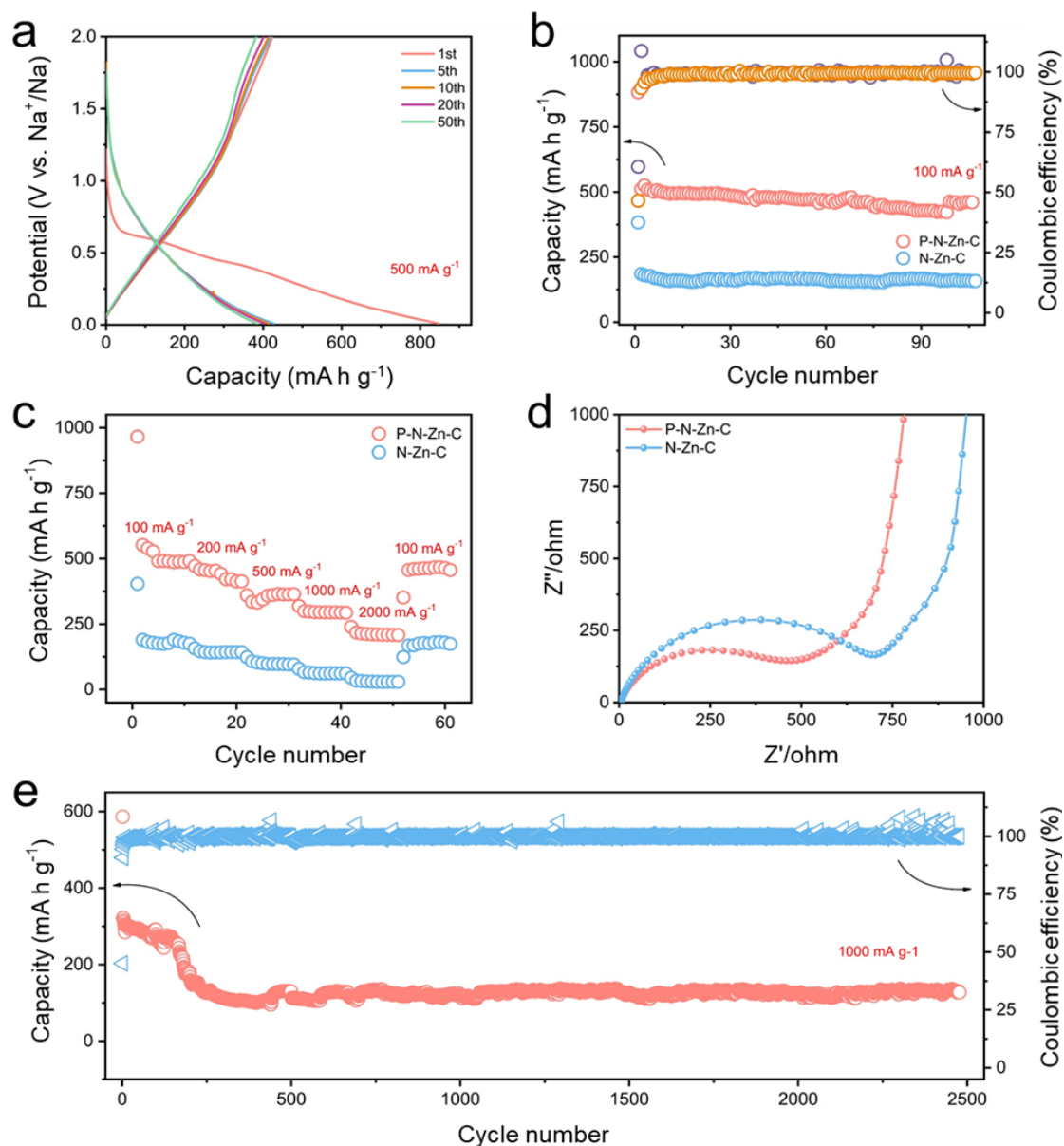
Figure 4. Electrochemical behavior of the as-prepared composites for sodium-ion storage. (a) Galvanostatic discharge/charge profiles of the first three, 5th, 10th, 20th, and 50th cycles of the P-N-Zn-C electrode at the current density of 500 mA g^{-1}. (b) Cycling performance of the P-N-Zn-C and N-Zn-C electrodes at the current density of 100 mA g^{-1}. (c) Rate capabilities at different current densities of the P-N-Zn-C and N-Zn-C electrodes. (d) Nyquist impedance plots of the P-N-Zn-C and N-Zn-C electrodes. (e) Cycling performance of the P-N-Zn-C electrodes at the high current density of 1000 mA g^{-1}.

Zn was removed from N-Zn-C (denoted as N-C) to investigate the function of Zn node in the composite. The electrochemical behaviors of N-C and N-Zn-C were evaluated by CV test at a scan rate of 0.1 mV s^{-1} between 0.01 and 2.0 V (vs. Na/Na$^+$). The CV curves of the N-C and N-Zn-C electrodes (**Figures S8a-b**) showed similar characteristics, which indicate the occurrence of similar electrochemical process during the sodiation/desodiation process. The result suggested that Zn in the composites does not take part in the electrochemical reactions during the sodiation/desodiation process. **Figure S9** investigates the cycle performances of the N-Zn-C and N-C electrodes at the current density of 100 mA g^{-1} for SIBs. The N-Zn-C and N-C electrodes can deliver initial charge capacities of 467.7 and 505.3 mA h g^{-1} in the initial cycle, respectively. These values present a high specific capacity based on the mass of carbon. The N-Zn-C electrode delivered a specific capacity of 203.67 mA h g^{-1} (based on the mass of carbon) whereas the N-C electrode delivered 132.5 mA h g^{-1} after 50 cycles. The decrease shows a substantial rapid capacity fade. The results clearly demonstrate that the N-Zn-C electrode exhibits a better cycle performance and the presence of Zn improves the stability of the composite during sodium storage process.

The rate capabilities of the P-N-Zn-C and N-Zn-C electrodes at different current densities are shown in **Figure 4c**. The initial discharge and charge capacities of the P-N-Zn-C electrode were 966 and 518.8 mA h g^{-1}, respectively. In comparison, the initial discharge and charge capacities of the N-Zn-C electrode (**Figure 4c**) were 403.8 and 177.8 mA h g^{-1}, respectively. The better performance of the P-N-Zn-C electrode indicates that P doping can efficiently enhance the integral electrical conductivity and

Na-ion transport of the composite. P doping can considerably suppress the deleterious reaction between the electrolyte and active materials.[61] In addition, the P-N-Zn-C electrode delivered discharge capacities of 486, 452, 361, 295, and 211 mA h g^{-1} at the current densities of 0.1, 0.2, 0.5, 1, and 2 A g^{-1}, respectively. Remarkably, the discharge capacity of the P-N-Zn-C electrode regained a value of 451 mA h g^{-1} after the 60th cycle when the current density was back to 100 mA g^{-1}. This finding signifies that the P-N-Zn-C electrode has a stable cycling performance and an excellent rate performance owing to its good chemical stability. By contrast, the N-Zn-C electrode exhibited discharge capacities of 189, 141, 98, 62, and 31 mA h g^{-1} at 0.1, 0.2, 0.5, 1, and 2 mA g^{-1}, respectively. The discharge capacity of the N-Zn-C electrode decreased to 170 mA h g^{-1} after switching back to 100 mA g^{-1} after 62 cycles. The results indicate the N-Zn-C electrode without P doping modification cannot accommodate the large volume expansion during electrochemical high-rate cycling and thus had a poor rate performance.

Further, the interfacial properties of the P-N-Zn-C, N-Zn-C, and N-C electrodes were investigated by electrochemical impedance spectroscopy (EIS) analysis as shown in **Figures 4d and S10-11**. The impedance spectra were recorded for fresh coin cells with the amplitude of 5.0 mV in a frequency range from 100 kHz to 0.01 Hz. As shown in the impedance graphs, the P-N-Zn-C electrode had a distinctly smaller charge-transfer resistance compared with the N-Zn-C electrode; thus, the P-N-Zn-C electrode had a higher charge transfer kinetics than the N-Zn-C electrode. As a result, the P-doped structure enabled the P-N-Zn-C electrode to become kinetically more favorable in

charge transfer. In the low-frequency region, the angles between the oblique lines with Z-axis for the P-N-Zn-C and N-Zn-C electrodes were larger than 45°, which indicate that the Na-ion intercalation in the as-prepared P-N-Zn-C electrode was not limited by the diffusion process. In other words, the EIS measurements demonstrate that the as-prepared P-N-Zn-C electrode is able to accommodate Na-ion diffusion through pseudocapacitive processes.[60] The solution ohmic resistances (R_s) of P-N-Zn-C, N-Zn-C, and N-C have similar internal resistances. However, the charge transfer resistance (R_{ct}) of the P-N-Zn-C electrode (430 Ω) film was markedly lower than those of the N-Zn-C (650 Ω) and N-C electrodes (880 Ω). These results suggest that the P-N-Zn-C electrode exhibited a lower electrochemical polarization and better electron transfer kinetics in the sodium intercalation process, which lead to a superior cycle performance, compared with the N-Zn-C and N-C composites.

Figure 4e displays the long-term cycling performance of the P-N-Zn-C electrode at the high current density of 1000 mA g^{-1}. The discharge capacity of the P-N-Zn-C electrode decreased to 428 mA h g^{-1} at the 13th cycle. The decay in capacity with cycling was probably caused by the detachment of the cracked active materials from conductive carbon or current collector and the increase in the impedance of the electrode from the SEI layer. The P-N-Zn-C electrode exhibited a reversible capacity of 130 mA h g^{-1} with a CE of 100% after 2500 cycles and thus exhibited superior cycling stability and rate capability for SIBs. The cycled structure of the P-N-Zn-C electrode before cycling and after 130 cycles are shown in **Figures S12a-d**). The P-N-Zn-C electrode was a 3-D polyhedral structure with a smooth surface before cycling (**Figures**

S12a-b). As shown in **Figures S12c-d**, the P-N-Zn-C electrode underwent substantial morphology change from a relatively smooth surface to a coarse and porous surface after the sodiation/desodiation processes. Notably, uniform nanoparticles of about 40 nm were observed on the surface of the P-N-Zn-C polyhedral structure. Such porous nanoparticles facilitate the diffusion of Na ions in the electrode and enables the achievement of durable high-rate capability.
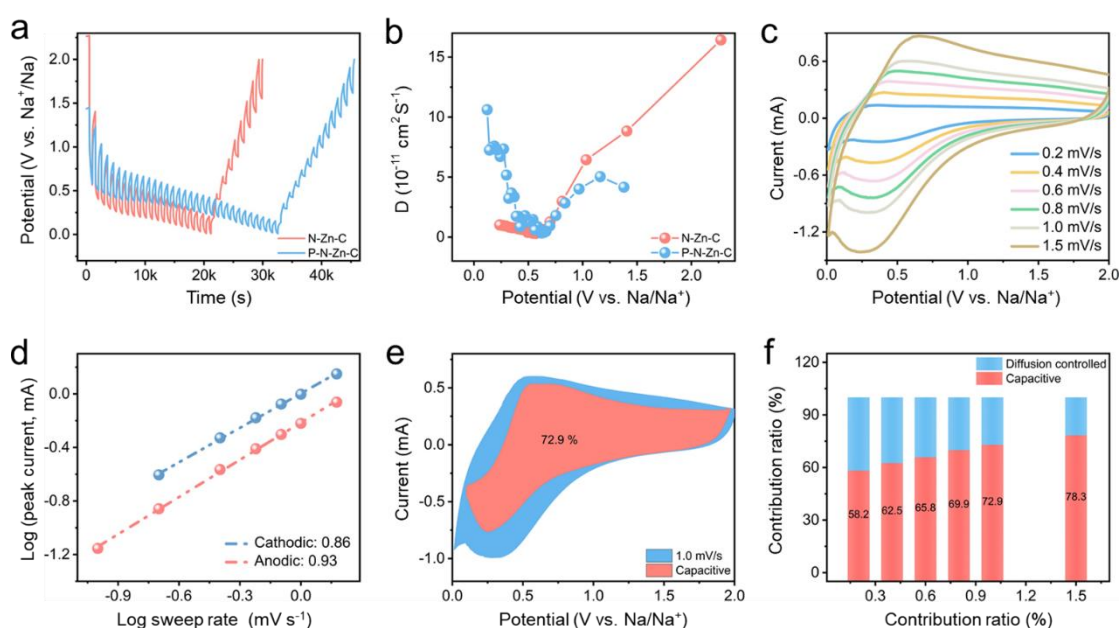

Figure 5. (a) GITT curves of the P-N-Zn-C and N-Zn-C electrodes versus Na/Na$^+$. (b) Chemical diffusion coefficients of Na ions in the P-N-Zn-C and N-Zn-C electrodes as a function of electrode potential obtained by GITT. (c) CV profiles at various scan rates from 0.2 mV s^{-1} to 1.5 mV s^{-1}. (d) Determination of *b* value using the relationship between peak current and sweep rate. (e) Separation of the total current (solid line) and capacitive currents (shaded regions) at 1.0 mV s^{-1}. (f) Contribution ratio of capacitive and diffusion-controlled charges at various scan rates.

The galvanostatic intermittent titration technique (GITT) is a well-known method for studying the solid-state ion diffusion mechanism and investigating the Na-

ion diffusivity in the electrode thin films for rechargeable SIBs. The P-N-Zn-C and N-Zn-C electrodes were fully discharged followed by a partial discharge at a current density of 100 mA g^{-1} and then an open circuit relaxation for 8 min for GITT measurements as displayed in **Figure 5a**. A single titration analysis curve at 0.583 V is shown in **Figure S13**. Different parameters, such as total cell voltage (ΔE_τ) and the change in equilibrium voltage (ΔE_s), were obtained from the single titration curve. The chemical diffusion coefficient of Na ions (D_{Na}) in the P-N-Zn-C and N-Zn-C electrodes were determined using Equations 1 and 2:

$$D_{Na} = \frac{4}{\pi\tau} \left(\frac{m_B V_M}{M_B A}\right)^2 \left(\frac{\Delta E_S}{\Delta E_\tau}\right)^2 , \left(\tau \ll \frac{L^2}{D_{Na}}\right); \quad (1)$$

$$D_{Na} = \frac{4}{\pi\tau} L^2 \left(\frac{\Delta E_S}{\Delta E_\tau}\right)^2 , \left(\tau \ll \frac{L^2}{D_{Na}}\right); \quad (2)$$

where m_B is the mass loading of the active material, V_M is the molar volume of the active material, M_B is the molar mass, A is the area of the electrode, L is the thickness of the electrode, τ is the time of periodic discharge/charge, ΔE_s is the voltage difference between the steady-state potentials before and after the current pulse, and ΔE_τ is the incremental voltage from the beginning to end of the current pulse. The D_{Na} of the P-N-Zn-C and N-Zn-C electrodes **(Figure 5b)** were calculated using Equation 1. The values obtained are plotted in **Figure 5a** as functions of cell voltage from 2.3 V to 0.01 V for discharging GITT analysis. The average D_{Na} value ranging is around 10^{-11} cm^2 s^{-1} was observed in the N-Zn-C electrode in the voltage range of 2.3-0.01 V, whereas the D_{Na} of the P-N-Zn-C electrode increased from 10^{-11} to 10^{-10} cm^2 s^{-1} in the same range. The enhanced D_{Na} caused by P doping increased the number of defects and active sites, which efficiently improved the sodium diffusion capability.

The kinetic analysis of the P-N-Zn-C electrode was investigated by separating the diffusion control capacity and capacitance-controlled capacity (details are provided in **Depiction S2**) to understand the pseudocapacitive behavior of the P-N-Zn-C electrode at high-rate performance. The CV curves (**Figure 5c**) have similar shapes with broad peaks during the cathodic and anodic scans at various scan rates from 0.2 mV s^{-1} to 1.5 mV s^{-1}. The unique P-N-Zn-C electrode showed obvious carbon material reactions in the CV curves at large scan rates. Hence, the cathodic and anodic b values for the P-N-Zn-C electrode of 0.93 and 0.86, respectively (**Figure 5d**), indicate a more favored capacitive kinetics. The capacitive contribution ratio enlarged with increasing scan rate and reached a maximum value of 72.9% at 1.0 mV s^{-1}. These results indicate its high pseudocapacitive sodium storage contribution to the whole capacity. Furthermore, the voltage profile shows the dominating capacitive contributions (red region) compared with the entire area (**Figure 5e**). The comparisons of the capacitive contribution ratio were nearly 58.2%, 62.5%, 65.8%, 69.9%, 72.9%, and 78.3% at 0.2, 0.4, 0.6, 0.8, 1.0, and 1.5 mV s^{-1} scan rates, respectively. This result shows a continuous increase in capacitive contribution with the increase in scan rates and suggests that pseudocapacitive contributes the main part of the whole capacity at high rate during the charging/discharging process.
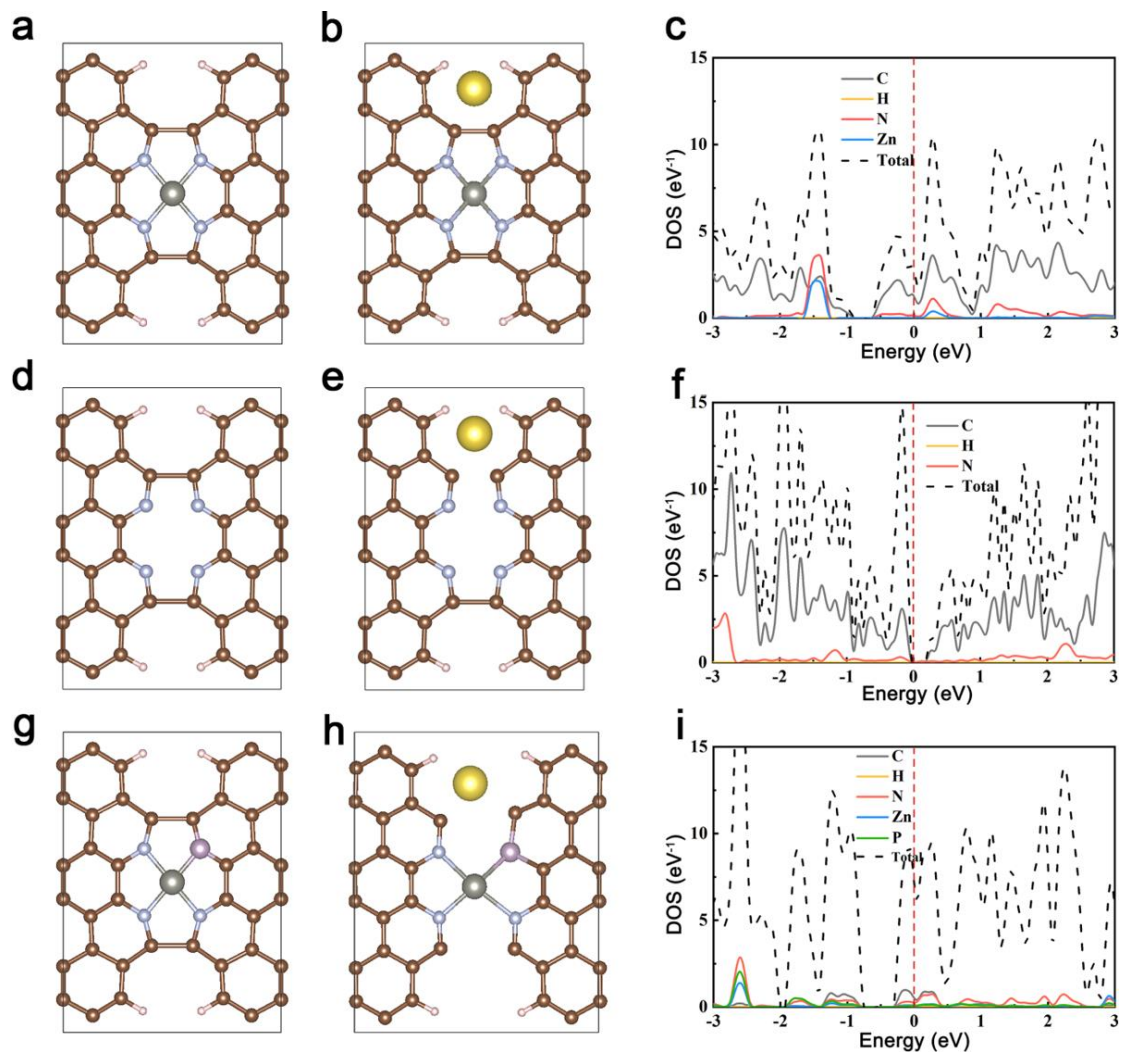
Figure 6. DFT calculation results of the composites. The optimized structure, the intercalation of Na on the optimized structure, and the corresponding DOS of the N-Zn-C (a-c), N-C (d-f), and P-N-Zn-C composites (g-i). Large yellow, gray, and red balls represent the Na, Zn, and P atoms, respectively. Small brown and blue balls represent the C and N atoms, respectively.

First-principle methods based on DFT were used to further investigate the interaction of P, N, and Zn on the electron distribution state in the composites. The most energy-favorable structures of the N-Zn-C, N-C and P-N-Zn-C layers were identified after various configurations were optimized with different doping sites as shown in

Figures 6a, d, and g. The computational results show that the Gibbs free energy of N-Zn-C is 0.7 eV lower than that of N-C; thus, N-Zn-C is more stable than N-C and Zn plays a role in the stability of the composite. P-N-Zn-C had the lowest Gibbs free energy (3.75 eV lower than that of N-Zn-C); therefore, P doping could further enhance the stability of the structure.

The binding energy of Na on the layer of the composite is important for the investigation of Na storage mechanism. The optimized configurations and binding energies, as well as distances of the sodium atoms from the surface of the composite, are shown in **Figure 6h**. The binding energy **(Figure 6b)** of Na on the N-Zn-C layer was -0.86 eV, which was lower than that of N-C (-0.52 eV). According to the calculations, P doping in N-Zn-C increased the strength of the interaction of Na atom on the P-N-Zn-C layer and resulted in a lower binding energy of -2.01 eV. The DFT results indicate that P and N doping and the presence of Zn atoms can substantially enhance the interaction of Na atom with carbon, and this finding is consistent with the experimental observations.

The density of state (DOS) of the composites was determined as shown in **Figures 6 c, f, and i** to investigate the electrical properties of the composites. Compared with the N-C composite, The N-Zn-C and P-N-Zn-C composites showed obvious electronic states across the Fermi energy level line and thus have a metallic nature and good electrical conductivity. In addition, the DOS value near the Fermi level gradually increased in the order: P-N-Zn-C > N-Zn-C > N-C **(Figures 6c, f, and i)**. This result indicates that P-N-Zn-C possesses the highest electron density, which facilities Na-ion

intercalation during the sodiation/desodiation processes. Theoretical calculations and further experimental studies confirmed that P and N doping and the existence of Zn node enhanced the reaction kinetics and improved the electrochemical property of SIBs.

In general, the P-N-Zn-C composite has shown excellent electrochemical performance because of four reasons. First, its porous polyhedral structure provides accessible interstitial sites and multiple open channels for electrolyte and Na-ion diffusion in the electrode material and also relieves the volume expansion during the sodiation/desodiation processes. Second, the unique P-N-Zn-C porous structure facilitates Na-ion storage in the interface and pores of the P-N-Zn-C electrode, which leads to the dominated pseudocapacitance behavior. Third, P and N dopants in the presence of Zn node can improve electronic conductivity, enhance structural stability, and create large amounts of defects, which provide additional reaction sites to accommodate Na ions.[5, 62]

4. CONCLUSIONS

In summary, well-defined P-N-Zn-C was synthesized from ZIFs through *in situ* carbonization to wrap and interconnect monodispersed Zn nanoparticles under Ar/H_2 atmosphere. The P-N-Zn-C composite inherited the porous polyhedral carbon structure of the ZIF-8 skeleton and demonstrated superior electrochemical performance as a potential anode material for SIBs compared with N-C. The remarkable synergistic effects and chemical and structural properties of the P-N-Zn-C composite gave rise to its superior electrochemical performance for sodium storage. The DFT results indicate that P and N doping and the presence of Zn atoms can remarkably enhance the

interaction of Na ions during sodiation/desodiation. The designed strategy of the P-N-Zn-C composite could be applied for other carbon materials for electrochemical energy conversion and storage technology.

■ **ASSOCIATED CONTENT**

Supporting Information: The SEM, XRD studies, N_2 adsorption-desorption isotherm and Pore distribution studies, TGA, XPS survey spectra, FTIR spectra studies, CV curves, cycling performance, Nyquist plot equivalent circuit studies.

■ REFERENCES:

1. Yin, H.; Yu, X.-X.; Zhao, H.; Li, C.; Zhu, M.-Q. Towards high-performance cathode materials for lithium-ion batteries: Al_2O_3-coated $LiNi_{0.8}Co_{0.15}Zn_{0.05}O_2$. *J. Solid State Electrochem.* **2018,** *22* (8), 2395-2403.

2. Yin, H.; Shen, W.; Qu, H.-Q.; Li, C.; Zhu, M.-Q. Boosted charge transfer and Na-ion diffusion in cooling-fins-like Sb_2Te_3-Te nano-heterostructure for long cycle life and high rate capability anode. Nano Energy **2020**, *70*, 104468.

3. Slater, M. D.; Kim, D.; Lee, E.; Johnson, C. S. Sodium-ion batteries. *Adv. Funct. Mater.* **2013,** *23* (8), 947-958.

4. Yin, H.; Yu, X. X.; Li, Q. W.; Cao, M. L.; Zhang, W.; Zhao, H.; Zhu, M. Q. Hollow porous CuO/C composite microcubes derived from metal-organic framework templates for highly reversible lithium-ion batteries. *J. Alloy. Compd.* **2017,** *706*, 97-102.

5. Yang, J.; Zhou, X.; Wu, D.; Zhao, X.; Zhou, Z. S-doped N-rich carbon nanosheets with expanded interlayer distance as anode materials for sodium-ion batteries. *Adv Mater* **2017,** *29* (6), 1604108.

6. Wu, L.; Hu, X. H.; Qian, J. F.; Pei, F.; Wu, F. Y.; Mao, R. J.; Ai, X. P.; Yang, H. X.; Cao, Y. L. Sb-C nanofibers with long cycle life as an anode material for high-performance sodium-ion batteries. *Energy Environ. Sci.* **2014,** *7* (1), 323-328.

7. Zheng, Y.; Wang, G. J. N.; Kang, J.; Nikolka, M.; Wu, H. C.; Tran, H.; Zhang, S.; Yan, H.; Chen, H.; Yuen, P. Y.; Mun, J.; Dauskardt, R. H.; McCulloch, I.; Tok, J. B. H.; Gu, X.; Bao, Z. An intrinsically stretchable high-performance polymer semiconductor with low crystallinity. *Adv. Funct. Mater.* **2019,** *29* (46), 1905340.

8. Prabakar, S. J.; Hwang, Y. H.; Bae, E. G.; Shim, S.; Kim, D.; Lah, M. S.; Sohn, K. S.; Pyo, M. SnO_2/graphene composites with self-assembled alternating oxide and amine layers for high Li-storage and excellent stability. *Adv Mater* **2013,** *25* (24), 3307-3312.

9. Zhou, X.; Wan, L. J.; Guo, Y. G. Binding SnO_2 nanocrystals in nitrogen-doped graphene sheets as anode materials for lithium-ion batteries. *Adv Mater* **2013,** *25* (15), 2152-2157.

10. Sun, Y.; Zhao, L.; Pan, H.; Lu, X.; Gu, L.; Hu, Y.-S.; Li, H.; Armand, M.; Ikuhara,

Y.; Chen, L. Direct atomic-scale confirmation of three-phase storage mechanism in $Li_4Ti_5O_{12}$ anodes for room-temperature sodium-ion batteries. *Nat. Commun.* **2013,** *4,* 1870.

11. Yan, D.; Xu, X. T.; Lu, T.; Hu, B. W.; Chua, D. H. C.; Pan, L. K. Reduced graphene oxide/carbon nanotubes sponge: a new high capacity and long life anode material for sodium-ion batteries. *J. Power Sources* **2016,** *316,* 132-138.

12. Sun, J.; Lee, H. W.; Pasta, M.; Yuan, H. T.; Zheng, G. Y.; Sun, Y. M.; Li, Y. Z.; Cui, Y. A phosphorene-graphene hybrid material as a high-capacity anode for sodium-ion batteries. *Nat. Nanotechnol.* **2015,** *10* (11), 980-985.

13. Xu, J.; Wang, M.; Wickramaratne, N. P.; Jaroniec, M.; Dou, S.; Dai, L. High-performance sodium-ion batteries based on a 3D anode from nitrogen-doped graphene foams. *Adv Mater* **2015,** *27* (12), 2042-2048.

14. Yu, X.-X.; Wang, L.; Yin, H. Hierarchical heterojunction structures based-on layered Sb_2Te_3 nanoplate@rGO for extended long-term life and high-rate capability of sodium batteries. *Appl. Mater. Today* **2019,** *15,* 582-589.

15. Xiao, L. F.; Lu, H. Y.; Fang, Y. J.; Sushko, M. L.; Cao, Y. L.; Ai, X. P.; Yang, H. X.; Liu, J. Low-defect and low-porosity hard carbon with high coulombic efficiency and high capacity for practical sodium-ion battery anode. *Adv. Energy Mater.* **2018,** *8* (20), 1703238.

16. Yang, F. H.; Zhang, Z. A.; Du, K.; Zhao, X. X.; Chen, W.; Lai, Y. Q.; Li, J. Dopamine derived nitrogen-doped carbon sheets as anode materials for high-performance sodium-ion batteries. *Carbon* **2015,** *91,* 88-95.

17. Wang, S. Q.; Xia, L.; Yu, L.; Zhang, L.; Wang, H. H.; Lou, X. W. Free-standing nitrogen-doped carbon nanofiber films: integrated electrodes for sodium-ion batteries with ultralong cycle life and superior rate capability. *Adv. Energy Mater.* **2016,** *6* (7), 1502217.

18. Yin, H.; Qu, H. Q.; Liu, Z.; Jiang, R. Z.; Li, C.; Zhu, M. Q. Long cycle life and high rate capability of three dimensional $CoSe_2$ grain-attached carbon nanofibers for flexible sodium-ion batteries. *Nano Energy* **2019,** *58,* 715-723.

19. Yin, H.; Liu, Y.; Yu, N.; Qu, H. Q.; Liu, Z.; Jiang, R.; Li, C.; Zhu, M. Q. Graphene-

like MoS$_2$ nanosheets on carbon fabrics as high-performance binder-free electrodes for supercapacitors and Li-ion batteries. *ACS Omega* **2018**, *3* (12), 17466-17473.

20. Cao, M.; Tao, L.; Lv, X.; Bu, Y.; Li, M.; Yin, H.; Zhu, M.; Zhong, Z.; Shen, Y.; Wang, M. Phosphorus-doped TiO$_2$-B nanowire arrays boosting robust pseudocapacitive properties for lithium storage. *J. Power Sources* **2018,** *396*, 327-334.

21. Yin, H.; Li, Q.; Cao, M.; Zhang, W.; Zhao, H.; Li, C.; Huo, K.; Zhu, M. Nanosized-bismuth-embedded 1D carbon nanofibers as high-performance anodes for lithium-ion and sodium-ion batteries. Nano Res. **2017**, *10* (6), 2156-2167.

22. Guruprasad, K.; Maiyalagan, T.; Shanmugam, S. Phosphorus doped MoS$_2$ nanosheet promoted with nitrogen, sulfur dual doped reduced graphene oxide as an effective electrocatalyst for hydrogen evolution reaction. *ACS. Appl. Energ. Mater.* **2019**, *2* (9), 6184-6194.

23. Silva, T. L.; Cazetta, A. L.; Zhang, T.; Koh, K.; Silva, R.; Asefa, T.; Almeida, V. C. Nanoporous heteroatom-doped carbons derived from cotton waste: efficient hydrazine oxidation electrocatalysts. *ACS. Appl. Energ. Mater.* **2019**, *2* (3), 2313-2323.

24. Fu, L. J.; Tang, K.; Song, K. P.; van Aken, P. A.; Yu, Y.; Maier, J. Nitrogen doped porous carbon fibres as anode materials for sodium-ion batteries with excellent rate performance. *Nanoscale* **2014,** *6* (3), 1384-1389.

25. Yin, H.; Hui, K. S.; Zhao, X.; Mei, S.; Lv, X.; Hui, K. N.; Chen, J. Eco-friendly synthesis of self-supported N-doped Sb$_2$S$_3$-carbon fibers with high atom utilization and zero discharge for commercial full lithium-ion batteries. *ACS. Appl. Energ. Mater.* **2020**, *3* (7), 6897-6906.

26. Zhao, H.; Yin, H.; Yu, X.-X.; Zhang, W.; Li, C.; Zhu, M.-Q. In$_2$O$_3$ nanoparticles/carbon fiber hybrid mat as free-standing anode for lithium-ion batteries with enhanced electrochemical performance. *J. Alloy. Compd.* **2018,** *735*, 319-326.

27. Kataoka, F.; Ishida, T.; Nagita, K.; Kumbhar, V.; Yamabuki, K.; Nakayama, M. Cobalt-doped layered MnO$_2$ thin film electrochemically grown on nitrogen-doped carbon cloth for aqueous zinc-ion batteries. *ACS. Appl. Energ. Mater.* **2020**, *3* (5), 4720-4726.

28. Tao, H. C.; Xiong, L. Y.; Du, S. L.; Zhang, Y. Q.; Yang, X. L.; Zhang, L. L.

Interwoven N and P dual-doped hollow carbon fibers/graphitic carbon nitride: an ultrahigh capacity and rate anode for Li and Na ion batteries. *Carbon* **2017,** *122*, 54-63.

29. Lu, K.; Hu, Z. Y.; Ma, J. Z.; Ma, H. Y.; Dai, L. M.; Zhang, J. T. A rechargeable iodine-carbon battery that exploits ion intercalation and iodine redox chemistry. *Nat. Commun.* **2017,** *8* (1), 527.

30. Liu, Y.; Li, G.; Fu, J.; Chen, Z.; Peng, X. Strings of porous carbon polyhedrons as self-standing cathode host for high-energy-density lithium-sulfur batteries. *Angew Chem Int Ed* **2017,** *56* (22), 6176-6180.

31. Yin, P.; Yao, T.; Wu, Y.; Zheng, L.; Lin, Y.; Liu, W.; Ju, H.; Zhu, J.; Hong, X.; Deng, Z.; Zhou, G.; Wei, S.; Li, Y. Single cobalt atoms with precise N-coordination as superior oxygen reduction reaction catalysts. *Angew Chem Int Ed* **2016,** *55* (36), 10800-10805.

32. Huang, J.-W.; Cheng, Q.-Q.; Huang, Y.-C.; Yao, H.-C.; Zhu, H.-B.; Yang, H. Highly efficient Fe-N-C electrocatalyst for oxygen reduction derived from core-shell-structured $Fe(OH)_3$@zeolitic imidazolate framework. *ACS. Appl. Energ. Mater.* **2019,** *2* (5), 3194-3203.

33. Lin, Z.; Yang, Y.; Li, M.; Huang, H.; Hu, W.; Cheng, L.; Yan, W.; Yu, Z.; Mao, K.; Xia, G.; Lu, J.; Jiang, P.; Yang, K.; Zhang, R.; Xu, P.; Wang, C.; Hu, L.; Chen, Q. Dual graphitic-N doping in a six-membered C-ring of graphene-analogous particles enables an efficient electrocatalyst for the hydrogen evolution reaction. *Angew Chem Int Ed* **2019,** *58* (47), 16973-16980.

34. Patel, M. A.; Luo, F.; Khoshi, M. R.; Rabie, E.; Zhang, Q.; Flach, C. R.; Mendelsohn, R.; Garfunkel, E.; Szostak, M.; He, H. P-doped porous carbon as metal free catalysts for selective aerobic oxidation with an unexpected mechanism. *ACS Nano* **2016,** *10* (2), 2305-2315.

35. Some, S.; Kim, J.; Lee, K.; Kulkarni, A.; Yoon, Y.; Lee, S.; Kim, T.; Lee, H. Highly air-stable phosphorus-doped n-type graphene field-effect transistors. *Adv Mater* **2012,** *24* (40), 5481-5486.

36. Qin, D. C.; Liu, Z. Y.; Zhao, Y. Z.; Xu, G. Y.; Zhang, F.; Zhang, X. G. A sustainable route from corn stalks to N, P-dual doping carbon sheets toward high performance sodium-ion batteries anode. *Carbon* **2018,** *130*, 664-671.

37. Li, Z. F.; Bommier, C.; Sen Chong, Z.; Jian, Z. L.; Surta, T. W.; Wang, X. F.; Xing, Z. Y.; Neuefeind, J. C.; Stickle, W. F.; Dolgos, M.; Greaney, P. A.; Ji, X. L. Mechanism of Na-ion storage in hard carbon anodes revealed by heteroatom doping. *Adv. Energy Mater.* **2017,** *7* (18), 1602894.

38. Zheng, F.; Yang, Y.; Chen, Q. High lithium anodic performance of highly nitrogen-doped porous carbon prepared from a metal-organic framework. *Nat. Commun.* **2014,** *5*, 5261.

39. Chen, C.; Wen, Y.; Hu, X.; Ji, X.; Yan, M.; Mai, L.; Hu, P.; Shan, B.; Huang, Y. Na^+ intercalation pseudocapacitance in graphene-coupled titanium oxide enabling ultra-fast sodium storage and long-term cycling. *Nat. Commun.* **2015,** *6*, 6929.

40. Ma, X.; Wu, X.; Shen, P. Rational Design of $Na_4Fe_3(PO_4)_2(P_2O_7)$ Nanoparticles embedded in graphene: Toward fast sodium storage through the pseudocapacitive effect. *ACS. Appl. Energ. Mater.* **2018**, *1* (11), 6268-6278.

41. Bao, J. F.; Yang, S. Z.; Zhang, P. F. Mechanochemical redox-based synthesis of highly porous $Co_xMn_{1-x}O_y$ catalysts for total oxidation. *Chin. J. Catal.* **2020**, *41*, 1846-1854.

42. Xia, B. Y.; Yan, Y.; Li, N.; Wu, H. B.; Lou, X. W.; Wang, X. A metal-organic framework-derived bifunctional oxygen electrocatalyst. *Nat. Energy* **2016,** *1* (1), 15006.

43. Xu, H.; Liu, Y. T.; Qiang, T. T.; Qin, L. G.; Chen, J.; Zhang, P. G.; Zhang, Y.; Zhang, W.; Tian, W. B.; Sun, Z. M. Boosting sodium storage properties of titanium dioxide by a multiscale design based on MOF-derived strategy. *Energy Storage Mater.* **2019,** *17*, 126-135.

44. Li, C. X.; Dong, S. H.; Tang, R.; Ge, X. L.; Zhang, Z. W.; Wang, C. X.; Lu, Y. P.; Yin, L. W. Heteroatomic interface engineering in MOF-derived carbon heterostructures with built-in electric-field effects for high performance Al-ion batteries. *Energy Environ. Sci.* **2018,** *11* (11), 3201-3211.

45. Song, J. X.; Yu, Z. X.; Gordin, M. L.; Li, X. L.; Peng, H. S.; Wang, D. H. Advanced sodium ion battery anode constructed via chemical bonding between phosphorus, carbon nanotube, and cross-linked polymer binder. *ACS Nano* **2015,** *9* (12), 11933-11941.

46. Song, J. X.; Chen, S. R.; Zhou, M. J.; Xu, T.; Lv, D. P.; Gordin, M. L.; Long, T. J.; Melnyk, M.; Wang, D. H. Micro-sized silicon-carbon composites composed of carbon-coated sub-10 nm Si primary particles as high-performance anode materials for lithium-ion batteries. *J. Mater. Chem. A* **2014,** *2* (5), 1257-1262.

47. Mei, J.; He, T.; Zhang, Q.; Liao, T.; Du, A.; Ayoko, G. A.; Sun, Z. Carbon-phosphorus bonds-enriched 3D graphene by self-sacrificing black phosphorus nanosheets for elevating capacitive lithium storage. *ACS Appl. Mater. Inter.* **2020,** *12* (19), 21720-21729.

48. Chai, G.-L.; Qiu, K.; Qiao, M.; Titirici, M.-M.; Shang, C.; Guo, Z. Active sites engineering leads to exceptional ORR and OER bifunctionality in P, N Co-doped graphene frameworks. *Energy Environ. Sci.* **2017,** *10* (5), 1186-1195.

49. Li, H.; Xu, S. M.; Yan, H.; Yang, L.; Xu, S. Cobalt phosphide composite encapsulated within N, P-doped carbon nanotubes for synergistic oxygen evolution. *Small* **2018,** *14* (19), 1800367.

50. Li, R.; Wei, Z. D.; Gou, X. L. Nitrogen and phosphorus dual-doped graphene/carbon nanosheets as bifunctional electrocatalysts for oxygen reduction and evolution. *Acs Catal.* **2015,** *5* (7), 4133-4142.

51. He, J.; Lv, W.; Chen, Y.; Wen, K.; Xu, C.; Zhang, W.; Li, Y.; Qin, W.; He, W. Tellurium-impregnated porous cobalt-doped carbon polyhedra as superior cathodes for Lithium-Tellurium batteries. *ACS Nano* **2017,** *11* (8), 8144-8152.

52. Tao, L.; Guo, P.; Li, T.; Zhou, X.; Fu, Y.; Yu, C.; Ji, H.; Highly efficient mixed-metal spinel cobaltite electrocatalysts for the oxygen evolution reaction. *Chinese. J. Catal.* **2020***, 41,* 1855-1863.

53. Zhang, P.; Sun, F.; Xiang, Z.; Shen, Z.; Yun, J.; Cao, D. ZIF-derived in situ nitrogen-doped porous carbons as efficient metal-free electrocatalysts for oxygen reduction reaction. *Energy Environ. Sci.* **2014,** *7* (1), 442-450.

54. Lu, Z.; Wang, B.; Hu, Y.; Liu, W.; Zhao, Y.; Yang, R.; Li, Z.; Luo, J.; Chi, B.; Jiang, Z.; Li, M.; Mu, S.; Liao, S.; Zhang, J.; Sun, X. An isolated zinc-cobalt atomic pair for highly active and durable oxygen reduction. *Angew Chem Int Ed* **2019,** *58* (9), 2622-2626.

55. Zhang, X.; Zhao, Z.; Zhang, W.; Zhang, G.; Qu, D.; Miao, X.; Sun, S.; Sun, Z. Surface defects enhanced visible light photocatalytic H_2 production for Zn-Cd-S solid solution. *Small* **2016,** *12* (6), 793-801.

56. Zhang, C.; Wang, X.; Liang, Q.; Liu, X.; Weng, Q.; Liu, J.; Yang, Y.; Dai, Z.; Ding, K.; Bando, Y.; Tang, J.; Golberg, D. Amorphous phosphorus/nitrogen-doped graphene paper for ultrastable sodium-ion batteries. *Nano Lett.* **2016,** *16* (3), 2054-2060.

57. Fu, J. W.; Chen, Z. H.; Wang, M. H.; Liu, S. J.; Zhang, J. H.; Zhang, J. N.; Han, R. P.; Xu, Q. Adsorption of methylene blue by a high-efficiency adsorbent (polydopamine microspheres): kinetics, isotherm, thermodynamics and mechanism analysis. *Chem. Eng. J.* **2015,** *259*, 53-61.

58. Shangguan, H. H.; Huang, W.; Engelbrekt, C.; Zheng, X. W.; Shen, F.; Xiao, X. X.; Ci, L. J.; Si, P. C.; Zhang, J. D. Well-defined cobalt sulfide nanoparticles locked in 3D hollow nitrogen-doped carbon shells for superior lithium and sodium storage. *Energy Storage Mater.* **2019,** *18*, 114-124.

59. Chen, B. A.; Liu, E. Z.; He, F.; Shi, C. S.; He, C. N.; Li, J. J.; Zhao, N. Q. 2D sandwich-like carbon-coated ultrathin TiO_2@defect-rich MoS_2 hybrid nanosheets: synergistic-effect-promoted electrochemical performance for lithium ion batteries. *Nano Energy* **2016,** *26*, 541-549.

60. Zheng, F.; Yang, Y.; Chen, Q. High lithium anodic performance of highly nitrogen-doped porous carbon prepared from a metal-organic framework. *Nat. Commun.* **2014,** *5*, 5261.

61. Wang, R.; Wang, S.; Jin, D.; Zhang, Y.; Cai, Y.; Ma, J.; Zhang, L. Engineering layer structure of MoS_2-graphene composites with robust and fast lithium storage for high-performance Li-ion capacitors. *Energy Storage Mater.* **2017,** *9*, 195-205.

62. Li, J.-H.; Chen, Y.-C.; Wang, Y.-S.; Ho, W. H.; Gu, Y.-J.; Chuang, C.-H.; Song, Y.-D.; Kung, C.-W. Electrochemical evolution of pore-confined metallic molybdenum in a metal-organic framework (MOF) for all-MOF-based pseudocapacitors. *ACS. Appl. Energ. Mater.* **2020,** *3* (7), 6258-6267.

63. Lu, Z.; Wang, N.; Zhang, Y.; Xue, P.; Guo, M.; Tang, B.; Xu, X.; Wang, W.; Bai, Z.; Dou, S. Metal-organic framework-derived sea-cucumber-like FeS_2@C nanorods with

outstanding pseudocapacitive Na-ion storage properties. *ACS. Appl. Energ. Mater.* **2018**, *1* (11), 6234-6241.